

Fine Tuning of Electrical Characteristics of Inkjet Printed Graphene for Physical and Chemical Sensing

Hyun-June Jang, Rapti Ghosh, Wen Zhuang, Xiaoben Zhang, Yuqin Wang, Xiaoao Shi, Xingkang Huang, Haihui Pu, Byunghoon Ryu, Janan Hui, Mark C. Hersam, and Junhong Chen*



Cite This: *ACS Appl. Mater. Interfaces* 2025, 17, 12911–12920



Read Online

ACCESS |

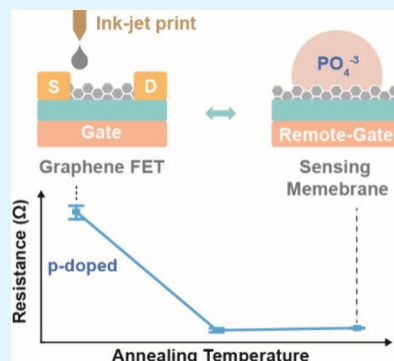
Metrics & More

Article Recommendations

Supporting Information

ABSTRACT: This study highlights the versatile applications of inkjet-printed graphene/ethyl cellulose (EC) in various electronic devices. Key points include its p-type doping achieved through low-temperature annealing, its use as a temperature sensor at higher annealing temperatures, and its effectiveness in electrochemical sensing, such as phosphate detection. The precise tuning of the oxygen composition of EC in graphene via thermal annealing was crucial to these capabilities. Electrical characterization showed consistent p-type doping behavior in graphene/EC annealed at 200 °C across all inkjet-printed graphene field-effect transistors. Upon annealing at 400 °C, the conductive properties of graphene were used in a hand-held reader device, demonstrating reversible responses to temperature fluctuations from 20 to 115 °C with a linearity of 99.8%. Furthermore, integrating inkjet-printed graphene electrodes annealed at 600 °C into remote floating-gate field-effect transistors resulted in a notably low detection limit of 1 pg/mL for phosphate ions in water, maintaining a linear response from 1 pg/mL to 10 ng/mL with a linearity of 98.91%. These applications underscore the adaptability and precision of inkjet-printed graphene, solidifying its role in advancing electronic components across various technological fields.

KEYWORDS: *graphene, inkjet printing, conductive ink, temperature sensing, phosphate detection*



INTRODUCTION

In recent years, the convergence of advanced materials and cutting-edge manufacturing techniques^{1–3} has propelled a revolution in electronic devices, particularly within the realms of sensory systems,⁴ electrochemical sensing,^{5,6} and biosensing applications.⁷ Graphene, renowned for its remarkable electrical, thermal, and mechanical properties, has emerged as a frontrunner in this dynamic field. With its exceptional electrical conductivity and atomic thinness, graphene stands out as an optimal material for crafting flexible and transparent electronic components tailored for a wide array of sensing applications.⁸

Two-dimensional (2D) materials have emerged as highly promising candidates for the post-Moore era, with significant potential in areas like integrated circuits and next-generation computing.^{9,10} 2D materials such as graphene demonstrate remarkable heterogeneity and compatibility with silicon and other 2D materials.⁹ These materials also offer remarkable surface-to-volume ratios and surface activities, rendering them highly suitable for sensing applications within the More than Moore domain.

Traditionally, graphene is synthesized through thermally intensive methods such as chemical vapor deposition (CVD),¹¹ which typically necessitates temperatures around 1,000 °C for graphene growth, and the thermal decomposition of silicon carbide,¹² yielding high crystalline quality graphene

with minimal defects. However, the elevated thermal requirements of these processes limit the choice of substrates suitable for direct graphene growth, and a subsequent transfer process of graphene is often necessary for device fabrication, e.g., on flexible plastic substrates.¹³ This limitation has spurred research into lower-temperature graphene production techniques to maintain functionality while broadening substrate compatibility.

Liquid-phase exfoliation (LPE) has emerged as the primary method for mass-producing two-dimensional materials like graphene, balancing quality and cost effectively.¹⁴ This process, driven by ultrasound forces and interactions with solvent molecules like ethyl cellulose (EC), produces stable graphene inks vital for additive manufacturing applications.¹⁵ EC serves a dual role in this process, stabilizing graphene dispersions in ethanol and tuning ink rheological properties. Additionally, EC weakens the van der Waals forces between graphite layers, facilitating the separation of graphene sheets into individual flakes suitable for further processing.

Received: December 6, 2024

Revised: January 27, 2025

Accepted: February 2, 2025

Published: February 11, 2025



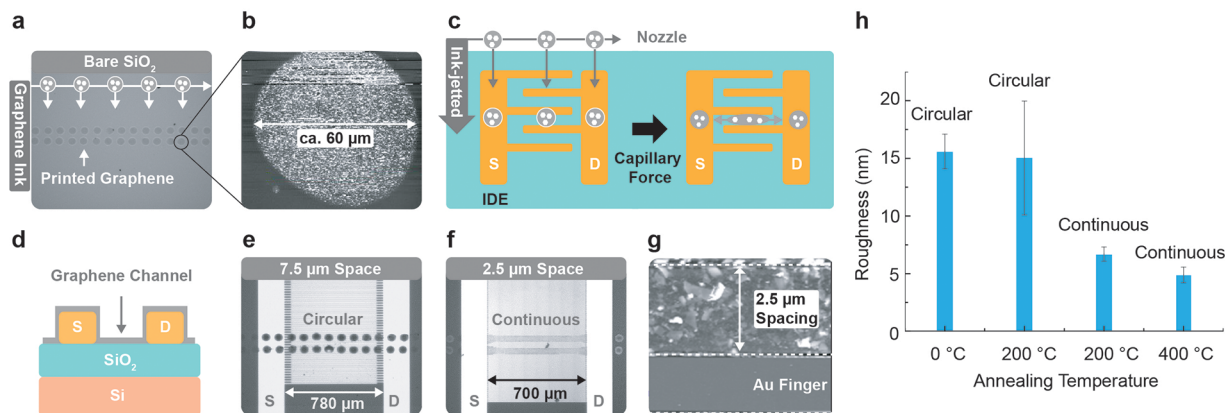


Figure 1. (a) Microscopic and (b) AFM images of inkjet-printed graphene on a bare SiO_2 substrate. Graphene is jetted from a nozzle, shaping a circular dot with a diameter of 60 nm on the bare SiO_2 surface. (c) Schematic images of graphene inkjet printed onto the Au IDE to form a FET structure with the graphene channel. Capillary forces, provided by microstructures of the IDE, create a continuous film of graphene within the space between the fingers. (d) Cross-sectional images of the GFET on the IDE. Microscopic images of inkjet-printed graphene on the IDE with (e) 7.5 μm and (f) 2.5 μm spacing between fingers. (g) AFM images of continuous graphene within the IDE with 2.5 μm spacing between fingers. (h) Roughness measured by AFM of inkjet-printed graphene to form a dot and a film within the IDE with and without annealing.

Inkjet printing, celebrated for its precision, scalability, and cost-effectiveness, is an ideal platform for depositing graphene produced through the LPE process onto various substrates with tailored designs.^{16–19} This technology opens up a plethora of applications in sectors such as flexible electronics,²⁰ displays,²¹ energy cells,^{22,23} sensors,²⁴ and transparent electrodes.²⁵ Its noncontact, digitally controlled deposition method enables the creation of intricate patterns and functional circuits with potential for submicron resolution,²⁶ which is essential for advanced electronic devices and sensors. Inkjet-printed graphene is notable for its low electrical resistivity (4 m Ω ·cm), high chemical and thermal stability, uniform morphology, compatibility with flexible substrates, and robust tolerance to bending stresses.²⁷ Moreover, as an additive manufacturing technique, inkjet printing offers a sustainable, eco-friendly alternative to traditional top-down fabrication methods, significantly reducing material waste and energy consumption.²⁸ In addition, the absence of harsh chemicals in EC-based graphene ink formulations aligns well with the growing demand for green technologies in the electronics industry. By integrating inkjet printing with graphene/EC, this approach successfully overcomes the limitations often associated with traditional CVD techniques, facilitating the seamless fabrication of electronic devices that can adapt to various surfaces and geometries.²⁸

In this manuscript, we highlight the diverse applications of inkjet-printed graphene, focusing on three primary functionalities: 1) p-type doping, 2) thermally dependent charge transport characteristics for temperature sensors, and 3) capabilities as an electrochemical sensing electrode for phosphate detection. These advancements are driven by the precise control of oxygen composition of inkjet-printed graphene/EC, with annealing temperatures adjusted between 200 and 600 °C. In the first application, all inkjet-printed graphene field-effect transistors (a-GFETs), where graphene serves as the source, drain, and channel, maintained stable electrical properties for up to 50 days post-fabrication, by leveraging semiconducting property in the channel and quasi-metallic property in the source and drain (S/D) regions, respectively. In the second application, quasi-metallic graphene, integrated with a hand-held device, exhibited a

reversible linear response in conductivity to temperature changes, achieving a linearity of 98.49% from 20 to 100 °C. Additionally, the integration of inkjet-printed graphene electrodes annealed at 600 °C into remote floating-gate field-effect transistors (RFGFETs) demonstrated an exceptionally low detection limit (LOD) of 1 pg/mL for phosphate ions in water, which is 10^3 times lower than the LOD of commercial phosphate sensors. This versatile approach leverages the unique properties of graphene for diverse detection modalities, thereby establishing a generalizable platform for a variety of sensing applications.

RESULTS AND DISCUSSION

In this study, inkjet-printed graphene/EC is utilized for three distinct purposes by fine-tuning the electrical properties of graphene/EC through controlled annealing temperatures, as illustrated in Figure S1. Initially, it serves as p-type doped graphene, exhibiting gate-modulated electronic properties essential for tuning charge carrier dynamics in graphene field-effect transistors (GFETs). Second, it functions as a low-resistance electrode embedded in S/D regions of GFETs, facilitating a-GFET configurations. Additionally, this quasi-metallic graphene has been explored for its temperature sensing applications. In the final section, the potential of graphene as an electrochemical sensing membrane was evaluated through phosphate detection. This multifaceted use of inkjet-printed graphene/EC not only showcases its versatility but also underscores its potential in advanced electronic and sensing technologies.

Inkjet Printing on Microstructure. The thickness of a graphene sheet in the graphene ink is approximately ~2 nm, with areas of ~200 nm by 100 nm (transmission electron microscopy image in Figure S2).¹⁹ In the inkjet printing process, a nozzle from the inkjet cartridge dispenses a precise 10 pL droplet of graphene/EC ink onto the substrate. This step is depicted in the microscopy images of printed graphene/EC on a SiO_2 surface as shown in Figure 1a. The resulting pattern on the SiO_2 surface forms a distinct circular shape, with an average diameter of 60 μm , as observed in the atomic force microscopy (AFM) image presented in Figure 1b. To reduce the roughness of the inkjet-printed graphene/EC channel, the

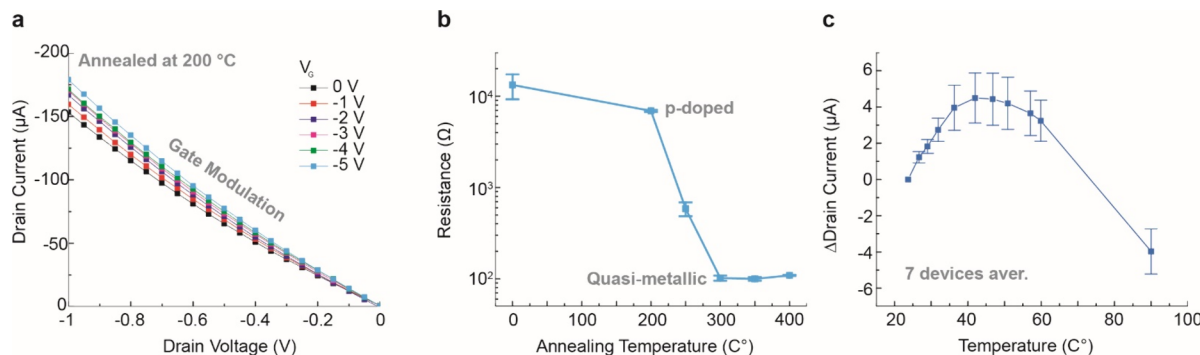


Figure 2. (a) Output curves of GFETs fabricated on Au IDE annealed at 200 °C. (b) Resistance change of graphene/EC channel in the IDE depending on annealing temperatures. (c) Drain current response of GFETs to increasing temperature over 7 GFETs.

microstructure of gold (Au) interdigitated electrodes (IDEs) was utilized (**Figure 1c**). In particular, capillary forces distribute the graphene ink uniformly along the pattern of S/D electrodes, significantly minimizing the surface roughness of the printed graphene by spreading across the microstructure defined by the IDEs. The final device geometry from this process is depicted in a cross-sectional schematic of the GFET on the IDE shown in **Figure 1d**.

To demonstrate the significance of this capillary effect to reduce the roughness of inkjet-printed graphene/EC, two distinct IDE designs were prepared, each featuring different dimensions of the fingers. Specifically, the width, spacing, and length of each finger in the IDE for the two designs were 2/2.5/780 μm (**Figure 1e**) and 5/7.5/700 μm (**Figure 1f**), respectively. The inkjet printer was programmed to leave 40 μm spacings between each droplet. Under the current printing conditions, the graphene/EC ink successfully filled six spaces, following the contour of the gold IDE fingers, without spreading into the unprinted areas (**Figure S3**). In contrast, the IDE with the larger spacing between fingers (**Figure 1e**) retained the circular-shaped morphology of the printed graphene/EC, similar to those seen on a plain SiO₂ surface, resulting from inadequate capillary action. Conversely, the IDE with narrower spacing between fingers (**Figure 1f**) facilitated the formation of a continuous graphene/EC film. This setup allowed the graphene/EC to span the gaps between IDE fingers, forming a seamless network as depicted in the AFM images of **Figure 1g**.

The AFM profile of the circular shaped graphene/EC on the SiO₂ surface reveals a root-mean-square (RMS) roughness of approximately 15.6 nm (**Figure S4a**). After annealing at 200 °C, the RMS roughness slightly decreases to 15 nm (**Figure 1h**). However, the standard deviation in RMS increases, attributed to the residue left from the EC after annealing, which contributes to this nonuniformity. Notably, when graphene/EC is structured by capillary forces of Au IDE, the roughness significantly decreases (**Figure S4b**), demonstrating values of 6.67 and 4.9 nm after annealing at 200 and 400 °C, respectively (**Figure 1h**).

Electronic Properties. The annealing temperature is a critical factor in controlling oxygen functional groups in inkjet-printed graphene/EC. These oxygen groups can serve as tunable parameters to engineer the intrinsic electronic and catalytic properties of graphene.²⁹ When graphene/EC printed on the Au IDE is annealed at 200 °C, it exhibits p-type doping, as evidenced by gate voltage modulation observed in both the output and transfer curves (**Figure 2a** and **S5**). Notably, during

these tests, neither gate leakage currents nor leakage currents between IDEs were observed (**Figure S5c**), and no S/D leakage currents were detected (**Figure S5d**). In single-layer graphene, both electrons and holes coexist due to its unique zero bandgap structure at the Dirac points, where conduction and valence bands meet. This allows them to behave as massless Dirac Fermions. However, graphene processed with EC at 200 °C undergoes p-type doping. Oxygen-containing functional groups such as epoxides and hydroxyls increase hole concentration and shift the Fermi level toward the valence band. This behavior is typical of graphene oxide, where oxygen groups induce p-type semiconducting properties.

It is noted that GFETs fabricated on Au IDEs with a 5 μm spacing between the fingers, incorporating graphene/EC annealed at 200 and 400 °C, do not exhibit gate modulation (**Figure S6**). This suggests that the thickness of the graphene/EC and the contact quality at the interface are crucial to achieving p-doped behavior. That is, adequate capacitance, ensured by sufficient contact between the graphene and the insulator, is necessary for effective gate modulation.

Gate modulation of the output curve was still observable 40 days after the initial fabrication, albeit weakened (**Figure S7a**). Drain current (I_D) levels of the GFETs remained stable for up to 40 days without any passivation layers on the graphene/EC channel (**Figure S7b**), underscoring the durability and long-term reliability of printed graphene/EC.

The resistance of the graphene/EC channel annealed at 200 °C was over 40 times higher than that of the channel annealed at temperatures above 300 °C, as shown in **Figure 2b**. An annealing temperature of 200 °C is sufficient to remove residual solvents, which enhances carrier mobility within the graphene. Additionally, at this temperature, the oxygen-containing groups in the EC begin to oxidize, exhibiting p-doped behavior of graphene/EC. GFETs subjected to annealing temperatures exceeding 300 °C displayed no discernible gate modulation in their transfer curves (**Figure S8a**) or output curves (**Figure S8b**), indicating the development of quasi-metallic properties in the graphene/EC.

To further elucidate the electronic properties of inkjet-printed graphene, an in-depth investigation into the thermal response of GFET conductivity was carried out, as detailed in **Figure 2c**. The I_D changes as a function of temperature exhibited a bell-shaped curve: the I_D increased with rising temperatures up to 45 °C, plateaued to 50 °C, and then displayed a decreasing I_D above 50 °C. To confirm the influence of non-ideal factors in the bell-shaped thermal response, hysteresis voltage was observed in the transfer curves

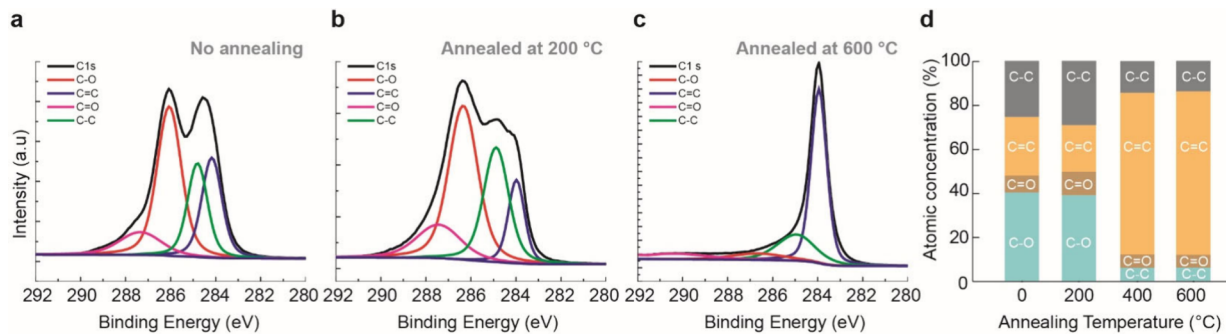


Figure 3. XPS spectra of graphene films depending on annealing conditions: (a) No annealing, (b) 200 °C, and (c) 600 °C. (d) Atomic composition changes of C-C, C=C, C=O, and C-O obtained from XPS spectra as a function of annealing temperature.

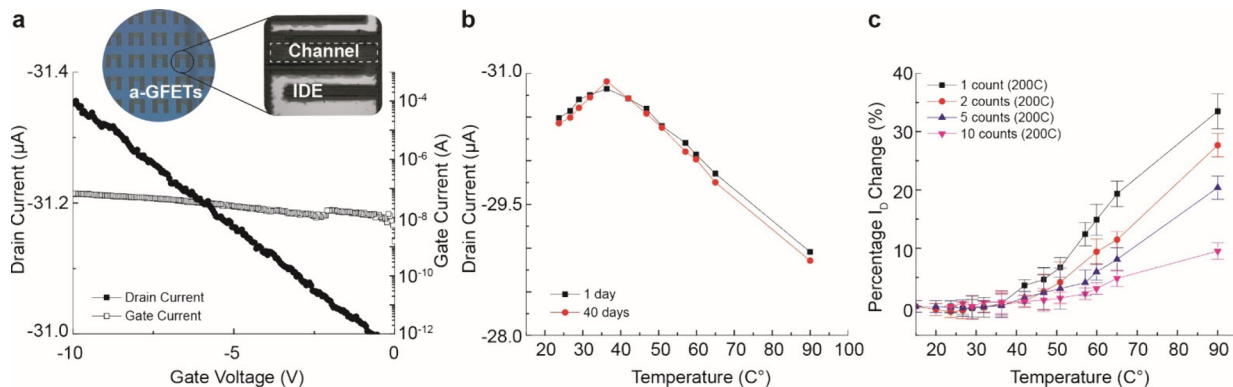


Figure 4. (a) Representative transfer curve of all inkjet-printed GFET. The inset of Figure 4a provides microscopy images showcasing arrays of all inkjet-printed GFETs on SiO₂ substrates with the graphene/EC channels neatly filled between the graphene IDEs. (b) The drain current response of these GFETs to temperature variations was methodically measured both 1 day and 40 days postfabrication. This analysis helps to evaluate the stability and consistency of the GFET electrical properties over time under thermal stress. (c) Drain current responses to temperature variations were also observed across GFETs with varying thicknesses of the graphene/EC layers, ranging from 1 to 10 layers. Each of these GFET configurations was annealed at 200 °C.

of GFET as the hot plate temperature increased (Figure S9). Hysteresis was measured using double-sweeping mode, and the hysteresis voltage remained consistently low, below 1 nA, across the entire temperature range. Notably, the linear response to temperature changes (Figure S10) is shown for GFETs annealed above 400 °C, which exhibit quasi-metallic properties. Therefore, the bell-shaped response curve in Figure 2c primarily reflects the intrinsic temperature response of the graphene/EC channel in the GFET, suggesting the presence of competing charge transport mechanisms. The increase in thermal energy up to 45 °C can likely be attributed to thermally activated charge transport through the graphene percolating network. However, beyond this temperature, increased lattice vibrations (phonons) and scattering mechanisms become dominant, leading to a reduction in the drain current levels. Notably, the few layers of inkjet-printed graphene, characterized by a high surface-to-volume ratio, appear to be particularly susceptible to phonon scattering, which is evident from the inflection points observed at low temperatures such as 50 °C.

X-ray photoelectron spectroscopy (XPS) provides insight into the chemical composition of inkjet-printed graphene/EC films subjected to different annealing temperatures. Without annealing, graphene/EC films include significant oxygen-containing functional groups such as C=O and C=O (Figure 3a). Some of these oxygen groups still remain on the graphene/EC even after annealing at 200 °C (Figure 3b). A rise in the annealing temperature above 400 °C (Figure S11)

and 600 °C (Figure 3c) significantly reduces oxygen-containing groups, showing almost identical atomic composition (Figure 3d). Similarly, Raman analysis indicated a reduction in oxygen-functional groups with increasing annealing temperature, as reflected by the I_D/I_G ratios of 0.71, 0.55, and 0.32 for graphene/EC without annealing, annealed at 200 °C, and annealed at 600 °C, respectively, and I_{D2}/I_G ratios of 0.68, 0.65, and 0.42 for the same conditions (Figure S12). These results suggest that EC undergoes complete thermal decomposition above 400 °C, predominantly leaving graphene. It is worth noting that such high annealing temperatures to reduce oxygen-containing groups can be reduced by adopting the photonic annealing method.³⁰

All Inkjet-Printed GFETs. To fully leverage inkjet printing technology for GFETs, a comprehensive approach was adopted by fabricating all components exclusively using inkjet-printed graphene. To this end, the original graphene/EC ink was diluted by 50% to precisely control the thickness of the printed graphene layers. The configuration of the IDE was meticulously designed, with each finger having dimensions of 100 μm in width, 100 μm in spacing, and 800 μm in length, as depicted in the inset of Figure 4a. By printing ten cycles of graphene/EC, a film thickness of 350 nm was achieved, verified by AFM in Figure S13. However, challenges arose with printing smaller IDE dimensions, where each finger measured 50/50/800 μm, and a small portion of short circuits developed between the IDE fingers (Figure S14). This observation is possibly due to the oversaturation of graphene/EC ink in the

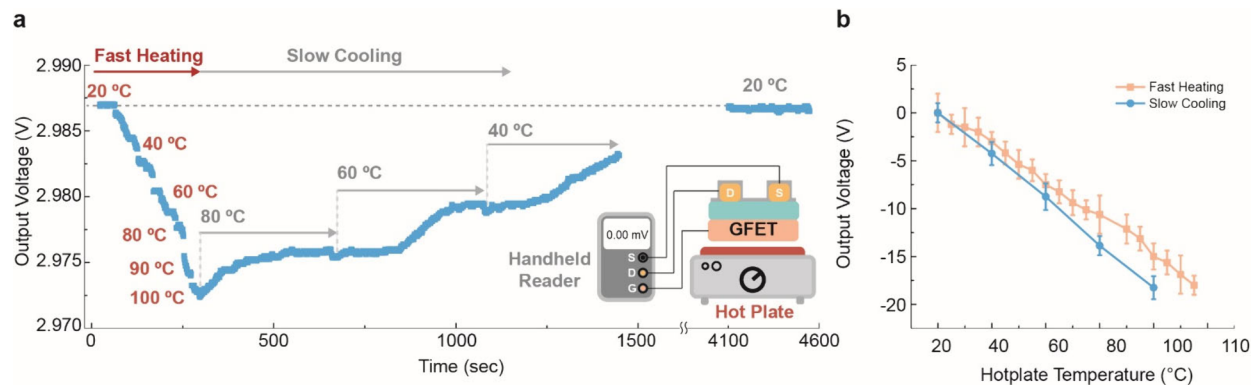


Figure 5. Hand-held temperature sensor integrated with GFET sensing components. (a) Real-time V_{out} response of the hand-held device to temperature variations of a hot plate in a range from 20 to 100 °C. (b) ΔV_{out} of the hand-held temperature sensor device versus hot plate temperature.

defined print area, exacerbated by the overlay of still-wet ink on the same patterns and the reduced spacing between dispensed droplets, which was adjusted to 20 μ m to ensure the formation of continuous graphene films. Ultimately, the printed IDE structure underwent annealing at 350 °C to preserve the quasi-metallic properties of graphene/EC, crucial for the S/D functions within the IDE.

The graphene channel, inkjet-printed between the IDEs as depicted in the inset of Figure 4a, underwent a crucial annealing process at 200 °C after being applied onto the previously annealed graphene IDE at 350 °C. This treatment led to clear gate modulation in the transfer curves of all inkjet-printed GFETs, with enhanced stability demonstrated by minimal drifts or hysteresis over 20 gate voltage double-sweep cycles, and no gate leakage current detected, as illustrated in Figure 4a. In contrast, annealing the graphene/EC channel at 350 °C resulted in all inkjet-printed GFETs exhibiting quasi-metallic properties, devoid of gate modulation effects in transfer curves, as depicted in Figure S15.

Additionally, a consistent temperature response curve related to the drain current of all inkjet-printed GFETs was observed in Figure 4b, closely resembling the behavior of GFETs on Au IDEs shown in Figure 2c, even 40 days postfabrication. Furthermore, no significant changes in drain current levels were noted, even without passivation layers, for up to 50 days after fabrication, as detailed in Figure S16. This robustness underscores the durability and reliability of inkjet-printed GFETs, showcasing their potential for long-term applications.

To explore the effect of varying thicknesses on the electrical properties of the graphene/EC channels, channels with thicknesses of approximately 12, 22, 100, and 350 nm were prepared, corresponding to 1, 2, 5, and 10 printing cycles, respectively, as measured by AFM (Figure S13). It was observed that while the drain current levels increased with the thickness of the graphene/EC channel, saturation occurred after just 2 printing cycles. This finding indicates that annealing temperature, which significantly affects resistance as shown in Figure 2b, is a more critical factor in determining charge transport properties than the channel thickness.

The impact of graphene thickness on temperature response, however, is clearly delineated in Figure 4c, where thinner graphene layers demonstrated a more pronounced percentage change in I_D in response to temperature variations. This heightened sensitivity is likely due to enhanced phonon

scattering effects, a result of their greater surface-to-volume ratios. It is noted that thicker graphene/EC channels, created through 5 and 10 printing cycles and annealed at 200 °C (Figure S17), exhibited deviations from the typical bell-shaped response, as depicted in Figures 2c and 4b. Instead, these thicker layers mirrored the behavior of quasi-metallic materials, where conductivity typically decreases with increasing temperature.

Temperature Sensing. Graphene's high thermal conductivity, sensitivity to temperature changes, and compatibility with flexible substrates make it a suitable material for temperature sensors,^{31–33} particularly in applications like wearable devices where flexibility and precision are important.

The resistance of graphene/EC stabilized at around 100 Ω at annealing temperatures above 300 °C, suggesting quasi-metallic properties (Figure 2b, S13) that exhibit a linear response to temperature variations, which is ideal for temperature sensors. Consequently, a GFET configured on an Au IDE and annealed at 400 °C, as shown in Figure S10, was chosen to demonstrate temperature sensing for hand-held device.

Initially, the GFET configured on an Au IDE and annealed at 400 °C was evaluated for its temperature detection capabilities under challenging conditions, including measurements in water as shown in Figure S18. This assessment aimed to ascertain the physical stability and robustness of the printed graphene/EC. The GFETs demonstrated no signs of the graphene/EC component detachment or dissolving into the solution, even when the hot-plate temperature reached 100 °C. Throughout the testing, there was a noticeable decrease in drain current with increasing hot plate temperature, indicative of a reduction in conductivity as temperatures rose. This observed behavior deviates from the typical bell-shaped curve usually seen at initial temperature increases, as illustrated in Figure 2c.

The GFET was successfully integrated with a hand-held reader device, as shown in Figure S19, specifically designed for temperature sensing applications. In this setup, the GFET served as the temperature sensing component positioned on a hot plate, with its connection to the hand-held device secured via an alligator clip. The hot plate's temperature was progressively increased from 20 to 100 °C in increments of 5 °C every 20 s, a process defined as fast heating. Once the temperature reached 100 °C, it was gradually allowed to decrease over a period of 400 s by 20 °C. The output voltage

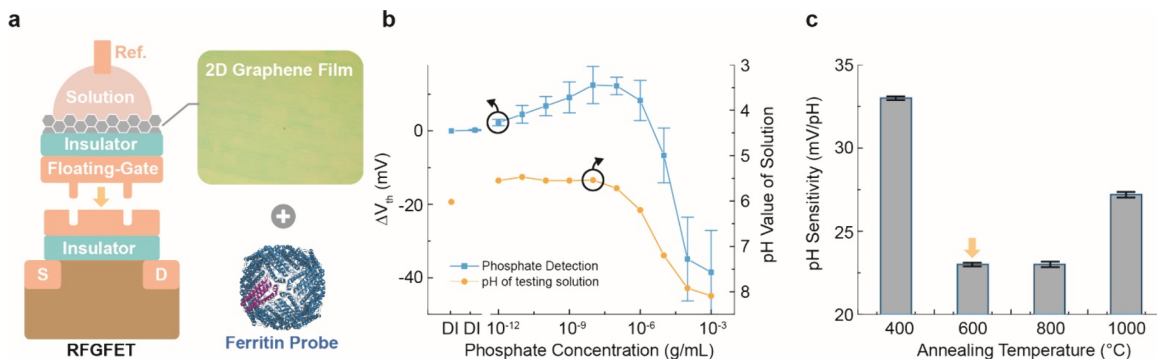


Figure 6. (a) RFGFET structure for electrochemical phosphate ion detection. (b) ΔV_{th} and pH versus phosphate ion concentrations. pH of phosphate ion solution was measured using a pH meter. (c) pH sensitivity of graphene sensing membranes with annealing temperatures in the range from 400 °C to 1000 °C.

(V_{out}), representing the drain current readout from the GFET, was amplified by an operational amplifier within the hand-held device. This output voltage was continuously measured at 1-s intervals, ensuring real-time monitoring and precise data capture.

Real-time changes in V_{out} due to fast heating and slow cooling are depicted in Figure 5a. During the fast heating phase, a decrease in V_{out} was noted as the temperature of the hot plate increased, indicating a reduction in the conductivity of metallic graphene due to rising temperatures. The temperature response of the device is also shown to be reversible, as illustrated in Figure 5b. The linearity of the temperature response was measured to be 98.52% during fast heating from 20 to 100 °C and increased to 99.8% during the slow cooling process. The use of inkjet printing enables customizable sensor designs and scalable fabrication, making it suitable for applications that demand accurate temperature monitoring and control in dynamic environments.

Phosphate Detection. Several studies have explored cost-effective electrochemical sensors based on inkjet-printed graphene for the detection of phosphate,³⁴ ammonium,³⁵ and various other ions.^{36,37} For instance, the reported LOD for phosphate using inkjet-printed GFETs is 6.2 ng/mL,³⁴ which is higher than the LOD of commercial phosphate sensors, typically achieving 2 ng/mL.³⁸ To improve both sensitivity and stability, we propose the use of an RFGFET configuration for inkjet-printed graphene (Figure 6a).

In remote floating-gate configuration, the graphene layer is electrically isolated by an insulator and confined to a very thin layer (approximately 12 nm) at the solution interface. This layer is capacitively connected to the gate of the FET transducer, effectively blocking any current flow into the graphene. This isolation prevents undesirable effects from interface traps, defects, and redox reactions, resulting in highly uniform threshold voltage levels that accurately reflect the intrinsic interfacial potentials of the graphene layer. Additionally, the thin graphene layer, with its high surface-to-volume ratio, further enhances the sensor's sensitivity to interfacial potential changes. Furthermore, graphene's biocompatibility and ease of functionalization significantly enhance its utility in sensing applications. The ability to form covalent bonds and engage in $\pi-\pi$ stacking interactions facilitates the attachment of a diverse array of biomolecules, polymers, and other chemical entities. This capability makes graphene an attractive choice for a sensing membrane, well-suited for various biosensing and electrochemical sensing applications.

Ferritin, functionalized on graphene, acts as a highly selective probe for capturing orthophosphate ions, attributed to the positive charge introduced onto the graphene membrane's surface.⁴¹ This positive charge arises from the specific binding interaction between ferritin and phosphate ions. As illustrated in Figure 6b, the detection of phosphate ions in water demonstrates a linear increase in signal from 1 pg/mL to 10 ng/mL, achieving a linearity of 98.91%. It is important to note that most conventional sensors and methods for detecting phosphate concentrations, such as colorimetric assays, electrochemical sensors, or enzymatic kits, typically have a LOD in the range of ng/mL to μ g/mL.⁴²

Beyond a concentration of 10 ng/mL, the signal plateaus, and a substantial decline is observed once concentrations exceed 100 ng/mL. This decrease is primarily due to negative surface potentials caused by pH changes in highly concentrated phosphate solutions. The initial pH of the testing solution, measured at 5.5, rises to 8.1 as phosphate concentrations reach 10 ng/mL. This increase in pH introduces negative charges, which counteract the positive surface potential changes induced by the ferritin-phosphate binding, thereby diminishing the detection signal.

To address pH-related disruptions affecting phosphate ion detection, a graphene film annealed at 600 °C, which demonstrates minimal pH sensitivity at 23 mV/pH, has been adopted as the preferred layer for the phosphate detection membrane (Figure 6c). Despite the high annealing temperatures, the inkjet-printed graphene retains a small amount of oxygen functional groups, as shown in Figure 3d. These groups primarily influence the detection curves of phosphate ions through pH interference.

Selectivity tests, presented in Figure S20, were conducted with various anions, including sulfate, chloride, and bicarbonate. Sample solutions at concentrations of 100 ng/mL and 1 μ g/mL, with DI water as the solvent, were prepared and measured using graphene/EC film functionalized with ferritin to assess ΔV_{th} , referred to as ΔV_{th} with ferritin. Since anion concentration influences pH, ΔV_{th} between 100 ng/mL and 1 μ g/mL was also measured for bare graphene/EC film (without ferritin) to account for pH-related ΔV_{th} changes, referred to as ΔV_{th} without ferritin. For phosphate only, ΔV_{th} with ferritin was larger than ΔV_{th} without ferritin, indicating that ferritin demonstrates high selectivity for phosphate detection (Figure S20).

Future efforts will focus on developing strategies to mitigate these effects. These strategies include deactivating the oxygen

groups on the graphene/EC electrode, incorporating a blocking layer, and employing calibration methods to compensate for pH variations. However, the varied pH of test samples in actual applications will alter phosphate ion sensitivity by affecting the isoelectric point of ferritin. Thus, a critical calibration step for interference is essential for a precise phosphate detection system. To achieve this, the sensor system must incorporate multiplexed detection capabilities that enable the measurement of various conditions of the testing solution, such as positive/negative controls, temperature, and pH. These features enhance calibration and minimize interference, broadening the dynamic range for accurate phosphate ion detection.

Nonetheless, the inkjet-printed graphene electrode in the RFGFET achieves an approximately 1 pg/mL LOD for phosphate ions— 10^3 times lower than commercial sensors—calculated using the 3-sigma rule (Figure 6b). These attributes establish the material as a highly sensitive electrode, well-suited for electrochemical sensing applications.

CONCLUSIONS

This study explores the broad potential of inkjet-printed graphene/EC, demonstrating its application across a range of sensing devices using a single graphene ink and inkjet printing technology to establish a generalizable platform for diverse electronic applications. By meticulously controlling printing parameters, fine-tuning the electrical and physical properties of graphene/EC through annealing and substrate structuring, and selecting various device architectures, we highlight the versatility and precision of this material, positioning it as essential for advanced electronic applications. Our electrical characterization revealed consistent p-type doping behavior in graphene/EC annealed at 200 °C across all inkjet-printed GFETs. Furthermore, GFETs annealed at 400 °C and integrated with a hand-held device displayed a reversible linear response in conductivity to temperature changes, achieving a linearity of 98.49% from 20 to 100 °C. Additionally, graphene annealed at 600 °C, optimized to minimize pH interference, was incorporated into an RFGFET structure, achieving a LOD for phosphate ions of 1 pg/mL— 10^3 times lower than commercial sensors. It maintained a linear response from 1 pg/mL to 10 ng/mL with a linearity of 98.91%. The adaptability and efficacy of inkjet-printed graphene make it a generalizable platform for diverse target analytes and sensing modalities.

EXPERIMENTAL PROCEDURES

Graphene Ink Formulation. Graphene/EC ink was produced according to previously described literature.^{27,43} Briefly, graphite powder purchased from Asbury Carbons (Micro 450) was dispersed in a solution of 1% w/v ethyl cellulose (4 cP, Sigma-Aldrich) in ethanol (200 proof, Decon Laboratories) at a concentration of 10% w/v. The resulting dispersion was transferred into a Starburst Labo wet jet milling instrument (Sugino Corp.) and operated at 200 MPa for 15 min or 10 exfoliation passes through the system. The exfoliated dispersion was then centrifuged (Avanti J-26XPI, Beckman Coulter) at 6,500 rpm for 30 min, and the supernatant was drawn and flocculated by adding 0.04 g/mL aqueous solution of NaCl in a 1:1.5 volume ratio and centrifuged at 7,000 rpm for 5 min. The supernatant was discarded and the flocculated sediment was washed with deionized water under vacuum filtration (0.2 μm MCE filter, Millipore Sigma) to remove any residual salt. The powder was dried and added to an 80:20 v/v cyclohexanone:terpineol solution at a

concentration of 25 mg/mL graphene/EC and bath sonicated overnight to achieve the final inkjet printable graphene ink.

The viscosity of the graphene/EC inks was measured at 9.98 ± 0.76 mPa/s at a shear rate of 100 s⁻¹, based on triplicate measurements, with the error bars representing the standard deviation (Figure S21). Measurements were conducted at room temperature using an Anton Paar Physica MCR 302 rheometer equipped with a CP 25-2 fixture and Peltier plate. The surface tension was measured at 32.41 ± 0.11 dyn/cm, with the displayed droplet image representing one of three trials, each using a volume of 13.4 μL. Surface tension measurements of the graphene/EC ink droplets were performed on a Kruss DSA100 Drop Shape Analyzer.

GFET Fabrication. 4-in. SiO₂ (300 nm)/Si wafer underwent standard cleaning procedures. Two Au IDE patterns were defined using a maskless aligner, with the width, space, and length of each finger in the IDE for the two designs being 2/2.5/780 μm and 5/7.5/700 μm, respectively. A 5 nm-thick TiO₂ layer and a 50 nm-thick Au layer were sequentially deposited by an e-beam evaporator, followed by the lift-off of the photoresist to achieve the IDE patterns. The patterned Au IDEs were annealed at 300 °C for 10 min in Ar gas. A Fuji film Dimatix DMP 2850 inkjet printer, equipped with a 10-pL cartridge (Fuji film Dimatix, DMC-11610) with a nozzle diameter of 21 μm, was used for inkjet printing. A slightly modified preprogrammed inverted trapezoid waveform with a jetting voltage of 20 V and a maximum jetting frequency of 5 kHz was utilized for ink deposition. The typical working distance between the nozzle and the substrate was 1 mm. To fabricate GFETs, the graphene channel was first printed on top of the Au IDE with 2.5 and 7.5 μm spacing between fingers. Drop spacing was optimized to be 40 μm for graphene flake deposition onto the substrate, which was heated to 50 °C to achieve GFETs in Figure 1f. One layer of graphene/EC was inkjet printed. Despite spaces between neighboring graphene droplets, capillary forces, facilitated by the microstructure of the Au IDE, ensured the formation of a continuous film between fingers (Figure 1c, 1f). This graphene IDE was further annealed at 200 °C for 10 min in Ar gas to remove residual additives in the inks. For temperature sensing applications, the graphene channel was annealed at 400 °C.

For the fabrication of all inkjet-printed GFETs, the original graphene/EC ink was diluted by 50% to precisely control the thickness of printed graphene layers. The drop spacing was also finely adjusted to 20 μm to ensure a continuous graphene network, which is critical for uniform current distribution and effective device performance. Initially, ten layers of graphene were inkjet-printed to form the graphene IDE, which is integral to the structure of the GFETs. The dimensions of each finger within the graphene IDE were standardized (width, spacing, and length: 100/100/800 μm). This graphene IDE layer was then annealed at 350 °C for 10 min under an argon gas atmosphere. This step is crucial for achieving the conductive properties of the graphene used in the S/D components and for removing any residues from the inks. Different thicknesses of graphene were achieved by varying the number of printing cycles, ranging from 1 to 10. To endow the GFETs with gate-tunable electronic properties, the graphene channel was annealed at 200 °C for 10 min under an argon gas atmosphere. The temperature response of the GFETs, as shown in Figures 2a-c, was measured on a hot plate. During the measurement, the actual temperature of the GFET devices was precisely monitored using an external thermometer attached to the same substrate as the GFETs.

Phosphate Detection. To fabricate an electrochemical graphene electrode, the cleaned 4-in. silicon wafer with a 300 nm-thick SiO₂ was treated with oxygen plasma for 5 min at 250 W under an O₂ flow rate of 10 sccm to introduce hydroxyl groups on SiO₂ surfaces. The wafer was fully immersed and incubated in a 5% (3-Aminopropyl) trimethoxysilane (APTMS) (Sigma-Aldrich, 281778) solution dissolved in ethanol (Sigma-Aldrich, 459836) for 2 h. After washing the surface, the wafer was heated at 120 °C for 20 min. One layer of graphene was inkjet-printed on the APTMS-treated SiO₂ surface with a 20 μm spacing between inkjetted droplets. The graphene film was sequentially annealed at 600 °C to reduce oxygen groups. Ferritin (Sigma-Aldrich, ferritin from equine spleen, #F4503) was function-

alized on the graphene surface by incubation in the ferritin solution (10 mg/mL) for 2 h to form a remote floating-gate electrode, which was connected to the gate of a commercial n-type metal-oxide-semiconductor field-effect transistor (MOSFET) (CD4007UB) using an alligator clip. A 20 μ L phosphate solution diluted in DI water was placed on the FRG. An Ag/AgCl reference electrode contacted the testing media solution to apply the gate bias in a range from 0 to 3 V for all measurements. All transfer curves were measured using a Keithley 4200A semiconductor analyzer with a source-drain voltage set at 50 mV, and the gate voltage fixed in the double-sweep mode.

■ ASSOCIATED CONTENT

SI Supporting Information

The Supporting Information is available free of charge at <https://pubs.acs.org/doi/10.1021/acsami.4c21469>.

Schematic diagrams of the device structures, TEM image of the graphene/EC nano flake, AFM image of the graphene/EC network, transfer curves and output curves of GFETs, correlation between the hysteresis voltage and the hot plate temperature, relationship between temperature and change in drain current, XPS data and Raman spectra for a graphene/EC, microscopy image of graphene/EC IDE, variations in drain current as a function of temperature, temperature detection in water, hand-held device components for temperature sensor, selectivity tests, and surface tension image ([PDF](#))

■ AUTHOR INFORMATION

Corresponding Author

Junhong Chen — Pritzker School of Molecular Engineering, University of Chicago, Chicago, Illinois 60637, United States; Chemical Sciences and Engineering Division, Physical Sciences and Engineering Directorate, Argonne National Laboratory, Lemont, Illinois 60439, United States; [orcid.org/0000-0002-2615-1347](#); Email: junhongchen@uchicago.edu

Authors

Hyun-June Jang — Pritzker School of Molecular Engineering, University of Chicago, Chicago, Illinois 60637, United States; Chemical Sciences and Engineering Division, Physical Sciences and Engineering Directorate, Argonne National Laboratory, Lemont, Illinois 60439, United States

Rapti Ghosh — Pritzker School of Molecular Engineering, University of Chicago, Chicago, Illinois 60637, United States; Chemical Sciences and Engineering Division, Physical Sciences and Engineering Directorate, Argonne National Laboratory, Lemont, Illinois 60439, United States

Wen Zhuang — Pritzker School of Molecular Engineering, University of Chicago, Chicago, Illinois 60637, United States; Chemical Sciences and Engineering Division, Physical Sciences and Engineering Directorate, Argonne National Laboratory, Lemont, Illinois 60439, United States

Xiaoben Zhang — Pritzker School of Molecular Engineering, University of Chicago, Chicago, Illinois 60637, United States; Chemical Sciences and Engineering Division, Physical Sciences and Engineering Directorate, Argonne National Laboratory, Lemont, Illinois 60439, United States; [orcid.org/0000-0001-5033-2642](#)

Yuqin Wang — Pritzker School of Molecular Engineering, University of Chicago, Chicago, Illinois 60637, United States; Chemical Sciences and Engineering Division, Physical Sciences and Engineering Directorate, Argonne National Laboratory,

Lemont, Illinois 60439, United States; [orcid.org/0000-0003-4444-2487](#)

Xiaobo Shi — Pritzker School of Molecular Engineering, University of Chicago, Chicago, Illinois 60637, United States; Chemical Sciences and Engineering Division, Physical Sciences and Engineering Directorate, Argonne National Laboratory, Lemont, Illinois 60439, United States

Xingkang Huang — Pritzker School of Molecular Engineering, University of Chicago, Chicago, Illinois 60637, United States; Chemical Sciences and Engineering Division, Physical Sciences and Engineering Directorate, Argonne National Laboratory, Lemont, Illinois 60439, United States

Haihui Pu — Pritzker School of Molecular Engineering, University of Chicago, Chicago, Illinois 60637, United States; Chemical Sciences and Engineering Division, Physical Sciences and Engineering Directorate, Argonne National Laboratory, Lemont, Illinois 60439, United States

Byunghoon Ryu — Department of Mechanical Engineering, Inha University, Incheon 22212, Republic of Korea

Janan Hui — Department of Materials Science and Engineering, Northwestern University, Evanston, Illinois 60208, United States

Mark C. Hersam — Department of Materials Science and Engineering, Department of Chemistry, and Department of Electrical and Computer Engineering, Northwestern University, Evanston, Illinois 60208, United States; [orcid.org/0000-0003-4120-1426](#)

Complete contact information is available at:
<https://pubs.acs.org/10.1021/acsami.4c21469>

Author Contributions

Electrical measurements, device fabrication, interpretation of data were carried out by H.-J. Jang, Y. Wang, W. Zhuang, X. Shi, and R. Ghosh. XPS was performed by R. Ghosh. AFM was measured by Y. Wang. IDEs were fabricated by X. Shi. The hand-held device was optimized by H.-J. Jang, B. Ryu, and W. Zhuang. Graphene ink was prepared by J. Hui and M. C. Hersam. TEM images were measured by X. Zhang. The manuscript was prepared by H.-J. Jang, J. Hui, H. Pu, X. Huang, M. C. Hersam, and J. Chen. All authors examined and commented on the manuscript. The project was guided by J. Chen.

Notes

The authors declare no competing financial interest.

■ ACKNOWLEDGMENTS

This work was primarily supported by the NSF Future Manufacturing Research Grant Program (NSF CMMI-2037026).

■ REFERENCES

- (1) Sui, X. Y.; Rangnekar, S. V.; Lee, J.; Liu, S. E.; Downing, J. R.; Chaney, L. E.; Yan, X. D.; Jang, H. J.; Pu, H. H.; Shi, X. A. Fully Inkjet-Printed, 2D Materials-Based Field-Effect Transistor for Water Sensing. *Adv. Mater. Technol.* **2023**, *8*, 2301288.
- (2) Zheng, W. R.; Lee, L. Y. S. Beyond sonication: Advanced exfoliation methods for scalable production of 2D materials. *Mater. Today* **2022**, *5* (2), 515–545.
- (3) Gamba, L.; Razzaq, M. E. A.; Diaz-Arauzo, S.; Hersam, M. C.; Bai, X. L.; Secor, E. B. Tailoring Electrical Properties in Carbon Nanomaterial Patterns with Multimaterial Aerosol Jet Printing. *ACS Appl. Mater. Interfaces* **2023**, *15* (49), 57525–57532.

- (4) Kim, J.; Lee, Y.; Kang, M.; Hu, L.; Zhao, S.; Ahn, J. H. 2D Materials for Skin-Mountable Electronic Devices. *Adv. Mater.* **2021**, *33* (47), 2005858.
- (5) Wanjari, V. P.; Reddy, A. S.; Duttagupta, S. P.; Singh, S. P. Laser-induced graphene-based electrochemical biosensors for environmental applications: a perspective. *Environ. Sci. Pollut. R.* **2023**, *30* (15), 42643–42657.
- (6) Wang, Y.; Guo, H. J.; Yuan, M.; Yu, J. B.; Wang, Z. P.; Chen, X. P. One-step laser synthesis platinum nanostructured 3D porous graphene: A flexible dual-functional electrochemical biosensor for glucose and pH detection in human perspiration. *Talanta* **2023**, *257*, 124362.
- (7) Ye, C.; Lin, C. T. Graphene-based nanocomposites for biosensors. *Microchim. Acta* **2023**, *190* (5), 183.
- (8) Qi, Y.; Sun, L.; Liu, Z. Super Graphene-Skinned Materials: An Innovative Strategy toward Graphene Applications. *ACS Nano* **2024**, *18*, 4617.
- (9) Liu, A. H.; Zhang, X. W.; Liu, Z. Y.; Li, Y. N.; Peng, X. Y.; Li, X.; Qin, Y.; Hu, C.; Qiu, Y. Q.; Jiang, H. The Roadmap of 2D Materials and Devices Toward Chips. *Nano-Micro Lett.* **2024**, *16* (1), 119.
- (10) Xiang, Y.; Shi, K.; Li, Y.; Xue, J.; Tong, Z.; Li, H.; Li, Z.; Teng, C.; Fang, J.; Hu, N. Active Micro-Nano-Collaborative Bioelectronic Device for Advanced Electrophysiological Recording. *Nanomicro Lett.* **2024**, *16* (1), 132.
- (11) Zhang, Y.; Zhang, L. Y.; Zhou, C. W. Review of Chemical Vapor Deposition of Graphene and Related Applications. *Acc. Chem. Res.* **2013**, *46* (10), 2329–2339.
- (12) Mishra, N.; Boeckl, J.; Motta, N.; Iacopi, F. Graphene growth on silicon carbide: A review. *Phys. Status Solidi A* **2016**, *213* (9), 2277–2289.
- (13) Chang, H. X.; Wang, G. F.; Yang, A.; Tao, X. M.; Liu, X. Q.; Shen, Y. D.; Zheng, Z. J. A Transparent, Flexible, Low-Temperature, and Solution-Processible Graphene Composite Electrode. *Adv. Funct. Mater.* **2010**, *20* (17), 2893–2902.
- (14) Li, Z. L.; Young, R. J.; Backes, C.; Zhao, W.; Zhang, X.; Zhukov, A. A.; Tillotson, E.; Conlan, A. P.; Ding, F.; Haigh, S. J.; et al. Mechanisms of Liquid-Phase Exfoliation for the Production of Graphene. *ACS Nano* **2020**, *14* (9), 10976–10985.
- (15) Yamuna, A.; Sundaresan, P.; Chen, S. M. Ethylcellulose assisted exfoliation of graphite by the ultrasound emulsification: An application in electrochemical acebutolol sensor. *Ultrason. Sonochem.* **2019**, *59*, 104720.
- (16) Zhou, X. Y.; Leng, T.; Pan, K. W.; Liu, Y.; Zhang, Z. R.; Li, J. S.; Novoselov, K. S.; Hu, Z. R. A sustainable approach towards printed graphene ink for wireless RFID sensing applications. *Carbon* **2024**, *218*, 118693.
- (17) Valayil Varghese, T.; Eixenberger, J.; Rajabi-Kouchi, F.; Lazouskaya, M.; Francis, C.; Burgoyne, H.; Wada, K.; Subbaraman, H.; Estrada, D. Multijet Gold Nanoparticle Inks for Additive Manufacturing of Printed and Wearable Electronics. *ACS Mater. Au* **2024**, *4* (1), 65–73.
- (18) Zhu, D. B.; Wang, Z. X.; Zhu, D. M. Highly Conductive Graphene Electronics by Inkjet Printing. *J. Electron. Mater.* **2020**, *49* (3), 1765–1776.
- (19) Torrisi, F.; Hasan, T.; Wu, W. P.; Sun, Z. P.; Lombardo, A.; Kulmala, T. S.; Hsieh, G. W.; Jung, S. J.; Bonaccorso, F.; Paul, P. J.; et al. Inkjet-Printed Graphene Electronics. *ACS Nano* **2012**, *6* (4), 2992–3006.
- (20) Shen, W. F.; Zhang, X. P.; Huang, Q. J.; Xu, Q. S.; Song, W. J. Preparation of solid silver nanoparticles for inkjet printed flexible electronics with high conductivity. *Nanoscale* **2014**, *6* (3), 1622–1628.
- (21) Wood, V.; Panzer, M. J.; Chen, J. L.; Bradley, M. S.; Halpert, J. E.; Bawendi, M. C.; Bulovic, V. Inkjet-Printed Quantum Dot-Polymer Composites for Full-Color AC-Driven Displays. *Adv. Mater.* **2009**, *21* (21), 2151.
- (22) Gaikwad, A. M.; Whiting, G. L.; Steingart, D. A.; Arias, A. C. Highly flexible, printed alkaline batteries based on mesh-embedded electrodes. *Adv. Mater.* **2011**, *23* (29), 3251–3255.
- (23) Hoth, C. N.; Choulis, S. A.; Schilinsky, P.; Brabec, C. J. High photovoltaic performance of inkjet printed polymer: Fullerene blends. *Adv. Mater.* **2007**, *19* (22), 3973.
- (24) Kulkarni, M. V.; Apte, S. K.; Naik, S. D.; Ambekar, J. D.; Kale, B. B. Ink-jet printed conducting polyaniline based flexible humidity sensor. *Sens. Actuat. B-Chem.* **2013**, *178*, 140–143.
- (25) Hassan, G.; Bae, J.; Lee, C. H. Ink-jet printed transparent and flexible electrodes based on silver nanoparticles. *J. Mater. Sci-Mater. El* **2018**, *29* (1), 49–55.
- (26) Capasso, A.; Del Rio Castillo, A.E.; Sun, H.; Ansaldi, A.; Pellegrini, V.; Bonaccorso, F. Ink-jet printing of graphene for flexible electronics: An environmentally-friendly approach. *Solid State Commun.* **2015**, *224*, 53–63.
- (27) Secor, E. B.; Prabhmirashi, P. L.; Puntambekar, K.; Geier, M. L.; Hersam, M. C. Inkjet Printing of High Conductivity, Flexible Graphene Patterns. *J. Phys. Chem. Lett.* **2013**, *4* (8), 1347–1351.
- (28) Michel, M.; Biswas, C.; Kaul, A. B. High-performance ink-jet printed graphene resistors formed with environmentally-friendly surfactant-free inks for extreme thermal environments. *Appl. Mater. Today* **2017**, *6*, 16–21.
- (29) Gao, Y. N.; Liu, L.; Jiang, Y.; Yu, D. X.; Zheng, X. M.; Wang, J. Y.; Liu, J. W.; Luo, D.; Zhang, Y. G.; Shi, Z. J. Design Principles and Mechanistic Understandings of Non-Noble-Metal Bifunctional Electrocatalysts for Zinc-Air Batteries. *Nano-Micro. Lett.* **2024**, *16* (1), 162.
- (30) Secor, E. B.; Ahn, B. Y.; Gao, T. Z.; Lewis, J. A.; Hersam, M. C. Rapid and Versatile Photonic Annealing of Graphene Inks for Flexible Printed Electronics. *Adv. Mater.* **2015**, *27* (42), 6683.
- (31) Kong, D.; Le, L. T.; Li, Y.; Zunino, J. L.; Lee, W. Temperature-Dependent Electrical Properties of Graphene Inkjet-Printed on Flexible Materials. *Langmuir* **2012**, *28* (37), 13467–13472.
- (32) Franco, M.; Alves, R.; Perinka, N.; Tubio, C.; Costa, P.; Lanceros-Mendéz, S. Water-Based Graphene Inks for All-Printed Temperature and Deformation Sensors. *ACS Applied. Electronic. Materials* **2020**, *2* (9), 2857–2867.
- (33) Wang, Z.; Gao, W.; Zhang, Q.; Zheng, K.; Xu, J.; Xu, W.; Shang, E.; Jiang, J.; Zhang, J.; Liu, Y. 3D-Printed Graphene/Polydimethylsiloxane Composites for Stretchable and Strain-Insensitive Temperature Sensors. *ACS Appl. Mater. Interfaces* **2019**, *11* (1), 1344–1352.
- (34) Bhat, K. S.; Nakate, U. T.; Yoo, J. Y.; Wang, Y.; Mahmoudi, T.; Hahn, Y. B. Nozzle-Jet-Printed Silver/Graphene Composite-Based Field-Effect Transistor Sensor for Phosphate Ion Detection. *ACS Omega* **2019**, *4* (5), 8373–8380.
- (35) Krivacic, S.; Bocek, Z.; Zubak, M.; Kojic, V.; Kassal, P. Flexible ammonium ion-selective electrode based on inkjet-printed graphene solid contact. *Talanta* **2024**, *279*, No. 126614.
- (36) He, Q.; Das, S. R.; Garland, N. T.; Jing, D.; Hondred, J. A.; Cargill, A. A.; Ding, S.; Karunakaran, C.; Claussen, J. C. Enabling Inkjet Printed Graphene for Ion Selective Electrodes with Postprint Thermal Annealing. *ACS Appl. Mater. Interfaces* **2017**, *9* (14), 12719–12727.
- (37) Pandhi, T.; Cornwell, C.; Fujimoto, K.; Barnes, P.; Cox, J.; Xiong, H.; Davis, P. H.; Subbaraman, H.; Koehne, J. E.; Estrada, D. Fully inkjet-printed multilayered graphene-based flexible electrodes for repeatable electrochemical response. *RSC Adv.* **2020**, *10* (63), 38205–38219.
- (38) Arvas, M. B.; Gorduk, O.; Gencen, M.; Sahin, Y. Preparation of a novel electrochemical sensor for phosphate detection based on a molybdenum blue modified poly(vinyl chloride) coated pencil graphite electrode. *Anal. Methods-Uk* **2019**, *11* (30), 3874–3881.
- (39) Jang, H. J.; Zhuang, W.; Sui, X.; Ryu, B.; Huang, X.; Chen, M.; Cai, X.; Pu, H.; Beavis, K.; Huang, J.; et al. Rapid, Sensitive, Label-Free Electrical Detection of SARS-CoV-2 in Nasal Swab Samples. *ACS Appl. Mater. Interfaces* **2023**, *15* (12), 15195–15202.
- (40) Jang, H. J.; Sui, X.; Zhuang, W.; Huang, X.; Chen, M.; Cai, X.; Wang, Y.; Ryu, B.; Pu, H.; Ankenbruck, N.; et al. Remote Floating-Gate Field-Effect Transistor with 2-Dimensional Reduced Graphene

Oxide Sensing Layer for Reliable Detection of SARS-CoV-2 Spike Proteins. *ACS Appl. Mater. Interfaces* **2022**, *14* (21), 24187–24196.

(41) Mao, S.; Pu, H. H.; Chang, J. B.; Sui, X. Y.; Zhou, G. H.; Ren, R.; Chen, Y. T.; Chen, J. H. Ultrasensitive detection of orthophosphate ions with reduced graphene oxide/ferritin field-effect transistor sensors. *Environ. Sci.-Nano* **2017**, *4* (4), 856–863.

(42) Mahmud, M. A. P.; Ejeian, F.; Azadi, S.; Myers, M.; Pejcic, B.; Abbassi, R.; Razmjou, A.; Asadnia, M. Recent progress in sensing nitrate, nitrite, phosphate, and ammonium in aquatic environment. *Chemosphere* **2020**, *259*, 127492.

(43) Chaney, L. E.; van Beek, A.; Downing, J. R.; Zhang, J. R.; Zhang, H. R.; Hui, J. N.; Sorensen, E. A.; Khalaj, M.; Dunn, J. B.; Chen, W. Bayesian Optimization of Environmentally Sustainable Graphene Inks Produced by Wet Jet Milling. *Small* **2024**, *20*, 2309579.

CAS INSIGHTS™

EXPLORE THE INNOVATIONS SHAPING TOMORROW

Discover the latest scientific research and trends with CAS Insights. Subscribe for email updates on new articles, reports, and webinars at the intersection of science and innovation.

[Subscribe today](#)

CAS
A division of the
American Chemical Society